Eur. Phys. J. A (2016) **52**: 172
DOI 10.1140/epja/i2016-16172-4

THE EUROPEAN PHYSICAL JOURNAL A

Regular Article – Experimental Physics

On the enhanced E1 transitions in the K = 3/2 parity doublet band in ^{223}Ra

H. Mach[1,2†], A. Lindroth[2], E. Ruchowska[1], J. Kvasil[3], B. Fogelberg[2], K. Gulda[4,1], A.J. Aas[5], M.J.G. Borge[6], I.S. Grant[7†], E. Hagebø[5], W. Kurcewicz[4,a], T. Martinez[8], B. Rubio[8], J.F. Smith[9,b], K. Steffensen[5], J.L. Tain[8], O. Tengblad[6,10], and T.F. Thorsteinsen[11]

[1] National Centre for Nuclear Research, BP1, Hoża 69, PL 00-681 Warsaw, Poland
[2] Department of Physics and Astronomy, Uppsala University, P.O. Box 516, SE-751 20 Uppsala, Sweden
[3] Department of Nuclear Physics, Charles University, V Holesovičkach 2, 18000 Prague 8, Czech Republic
[4] Faculty of Physics, University of Warsaw, Pasteura 5, PL 02-093 Warsaw, Poland
[5] Department of Chemistry, University of Oslo, P.O. Box 1033, Blindern, N-0315 Oslo, Norway
[6] Insto. De Estructura de la Materia, CSIC, E-28006 Madrid, Spain
[7] Schuster Laboratory, University of Manchester, Manchester M13 9PL, UK
[8] Insto. de Física Corpuscular, CSIC-Univ. Valencia, E-46100 Burjassot, Spain
[9] Oliver Lodge Laboratory, University of Liverpool, Liverpool, L69 7ZE, UK
[10] PPE Division, CERN, CH-1211 Geneva 23, Switzerland
[11] Department of Physics, University of Bergen, N-5007 Bergen, Norway

Received: 13 March 2016 / Revised: 17 May 2016
Published online: 24 June 2016

Communicated by R.K. Bhandari

Abstract. We have applied the fast timing $\beta\gamma\gamma$(t) technique to remeasure lifetimes of selected states in ^{223}Ra populated in the β^- decay of ^{223}Fr. $T_{1/2}$ = 587(12) ps and 210(13) ps have been obtained for the $3/2^-$ and $5/2^-$ states at 50.1 and 79.7 keV, that are more accurate than the previous values of 630(70) ps and 166(55) ps, respectively. Our $|D_0|$ value of 0.155(10) e·fm obtained for the $K = 3/2$ configuration together with the available values of $|D_0|$ for the $K = 1/2$ and $K = 5/2$ parity doublet bands establish the configuration dependence of $|D_0|$ at low spins in this nucleus. Results of theoretical calculations performed for ^{223}Ra, using the quasiparticle-phonon model (QPM) with inclusion of the Coriolis coupling, reasonably well reproduce octupole correlations in this nucleus.

1 Introduction

The ^{223}Ra isotope is a nucleus of considerable interest for many reasons. Firstly, it lies at the center of the octupole deformation region in the actinides and is predicted to be the most octupole deformed odd-A Ra nucleus. Secondly, it is placed in the ^{222}Ra-^{226}Ra region where values of the electric dipole moments D_0 are much lower than expected for the center of octupole region. Theory explains this by the quenching phenomenon, in which the cancellation between macroscopic and shell correction contributions to the D_0 moment takes place [1]. Finally, ^{223}Ra is one of a few nuclei in which considerably different electric dipole moments were determined for different configurations. The D_0 values of 0.079(5), 0.164(23) and 0.039(6) e·fm (based on lifetimes from refs. [2], [3,4] and [4]) were observed for the lowest spin levels of the $K = 1/2$, 3/2 and 5/2 configurations, respectively, implying a strong configuration dependence of the $E1$ strength. Theory predicts different octupole barrier heights [5] and slightly different D_0 values [1] for different single quasiparticle configurations in octupole deformed nuclei. However in ^{223}Ra, in contrast to experiment, the calculations of ref. [1] predict almost constant D_0 value of only ~ 0.04 e·fm for all three configurations. We have therefore undertaken experimental verification of D_0 moments in this nucleus.

Experimentally the ^{223}Ra nucleus was previously studied by ^{227}Th alpha decay [2,4,6] and by ^{223}Fr beta decay [7]. Interpretation of experimental data for ^{223}Ra has been performed by Sheline *et al.* in ref. [8]. Compilation of experimental data for this isotope is given in ref. [9]. Theoretical studies of ^{223}Ra have been performed in refs. [1, 5,8,10–13].

[a] e-mail: kurcewic@mimuw.edu.pl
[b] *Present address*: School of Engineering and Computing, University of the West Scotland, Paisley, PA1 2BE, UK.
[†] Deceased.

To verify the D_0 values in ^{223}Ra level lifetimes can be remeasured by modern high-resolution techniques now available. The half-life of the $3/2^-$ state at 50.1 keV was measured more than 50 years ago as 630(70) ps [3], but a different result of $T_{1/2} = 1070(130)$ ps was given in an internal report [14] and quoted in ref. [2]. Moreover, a rather imprecise level mean lifetime of $\tau = 240(80)$ ps ($T_{1/2} = 166(55)$ ps) was determined for the $5/2^-$ state at 79.7 keV in ref. [4] and it was adopted in *Nuclear Data Sheets* [9] as the half-life $T_{1/2}$ (also for higher levels the τ values of ref. [4] were adopted as $T_{1/2}$ in refs. [9,15]); this needs to be verified. In the present work we have remeasured lifetimes of selected states in ^{223}Ra using the advanced time-delayed $\beta\gamma\gamma$(t) method by Mach *et al.* [16, 17] at the PSB ISOLDE mass separator at CERN. These measurements are a part of our systematic investigation of the $E1$ strength in the actinide region [18–22].

Details of the present measurement and data analysis are given in sects. 2 and 3, while the discussion of the experimental results, and description of theoretical calculations with the quasiparticle-phonon model, are presented in sect. 4.

2 Experimental details

The measurements were performed at the ISOLDE facility at CERN using fast timing detectors that were precisely time calibrated at the OSIRIS fission-product mass separator in Studsvik. Levels in ^{223}Ra were populated in the β^- decay of ^{223}Fr via a decay chain from $^{223}\text{Rn} \rightarrow {}^{223}\text{Fr} \rightarrow {}^{223}\text{Ra}$. The activity of ^{223}Rn was produced by bombardment of a ThC_2 target with 1 GeV proton beam from the PS Booster. A highly pure beam of Rn was extracted from the target coupled to a plasma ion source via a cold transfer line. The beam was mass separated and deposited onto a movable magnetic tape at the measuring station, which was specially designed for the advanced time-delayed $\beta\gamma\gamma$(t) measurements [17]. A more detailed description of the experimental set-up has already been given in [18] (see, for example, fig. 1 in ref. [18]), so only a brief presentation is given below.

The set-up included four detectors positioned around the beam deposition point outside the experimental chamber; each of the four detectors is described below. The fast timing β-detector was a 3 mm thick ΔE NE111A plastic scintillator to ensure almost constant time response of the fast timing system, independent of the β-particle energies. It was placed behind the deposition tape and separated from it by a thin Al foil. The set of γ-ray detectors consisted of a small BaF_2 crystal for fast timing and two Ge detectors with efficiencies of 40% and 70%, respectively. A three-parameter time-delayed coincidence system was set between the β detector and each of the γ detectors. For data acquisition, a valid event required a coincidence between the β detector and any of the γ detectors. Up to seven parameters were collected per coincident event: the energy of the β particle, and two parameters (the energy of a γ-ray and the time delay between the β and γ-rays) for each coincident γ detector. In the off-line analysis the gate set on the β spectrum was chosen to keep the time response of the fast timing system constant in the whole range of selected β-particle energies.

The data were collected in the following way: first the beam was continuously deposited and the decay of ^{223}Rn to ^{223}Fr ($T_{1/2} = 24.3$ min) dominated the spectrum, then the beam was deflected and the sample was allowed to decay. In the second stage the spectrum was dominated by the decay of ^{223}Fr to ^{223}Ra ($T_{1/2} = 22.0$ min), but included also a small amount of events from the ^{223}Rn to ^{223}Fr decay. This collection process was repeated a few times.

The advanced time-delayed method requires that the time response of the fast timing detectors has been carefully calibrated (to a picosecond precision) for various types of γ-rays interactions in the crystal. It is also a requirement to check that the shape of time spectra for prompt radiation is close to the symmetric semi-Gaussians over the range of γ-ray energies of interest. In particular, the time calibration of the BaF_2 detector was obtained off-line at ISOLDE using a pre-calibrated source of $^{140}\text{Ba} \rightarrow {}^{140}\text{La} \rightarrow {}^{140}\text{Ce}$ that was prepared at the OSIRIS separator. A cross-check of time-calibration and symmetry for prompt response, was obtained *in situ* and in beam from transitions in the decays of $^{227}\text{Fr} \rightarrow {}^{227}\text{Ra}$ and $^{227}\text{Rn} \rightarrow {}^{227}\text{Fr}$ which were analyzed by both the slope and centroid shift methods [18,23]. More detailed time calibrations were done at OSIRIS using a variety of beams while maintaining the experimental geometry as close as possible to that at ISOLDE.

3 Analysis of fast timing $\beta\gamma$ events

The coincidence data were collected in a few batches. Each included a different ratio of events from the competing decays of $^{223}\text{Rn} \rightarrow {}^{223}\text{Fr}$ and $^{223}\text{Fr} \rightarrow {}^{223}\text{Ra}$. For the present analysis two batches were selected: one with a dominant ^{223}Fr to ^{223}Ra decay (batch-1), and a second one (batch-2, which was used in a correction procedure) with a dominant decay of ^{223}Rn to ^{223}Fr. Each batch of data was pre-sorted off-line into two separate blocks of $\beta\gamma$(t) coincidences: one corresponding to the β-Ge and the other to the fast timing β-BaF_2(t) coincidences, respectively. The number of β-Ge-BaF_2(t) coincidence events collected for the decay of ^{223}Fr to ^{223}Ra, was too small to warrant analysis. The β-Ge and β-BaF_2(t) blocks of data that were sorted from the same batch, contained the same ratio of events from the decays of $^{223}\text{Rn} \rightarrow {}^{223}\text{Fr}$ and $^{223}\text{Fr} \rightarrow {}^{223}\text{Ra}$. We used the first block of data, β-Ge, which included high-resolution Ge spectra, to determine this ratio for each batch of data. Then this information was used to deduce the necessary fraction of the batch-2 spectrum to be subtracted from the spectrum from batch-1 in order to provide a complete cancellation of the contribution from the impurity decay of $^{223}\text{Rn} \rightarrow {}^{223}\text{Fr}$.

Figure 1(a) shows the β-gated Ge spectrum for ^{223}Ra, purified from the $^{223}\text{Rn} \rightarrow {}^{223}\text{Fr}$ decay. A very strong presence of two γ-rays at 50.1 and 79.7 keV is a reflection

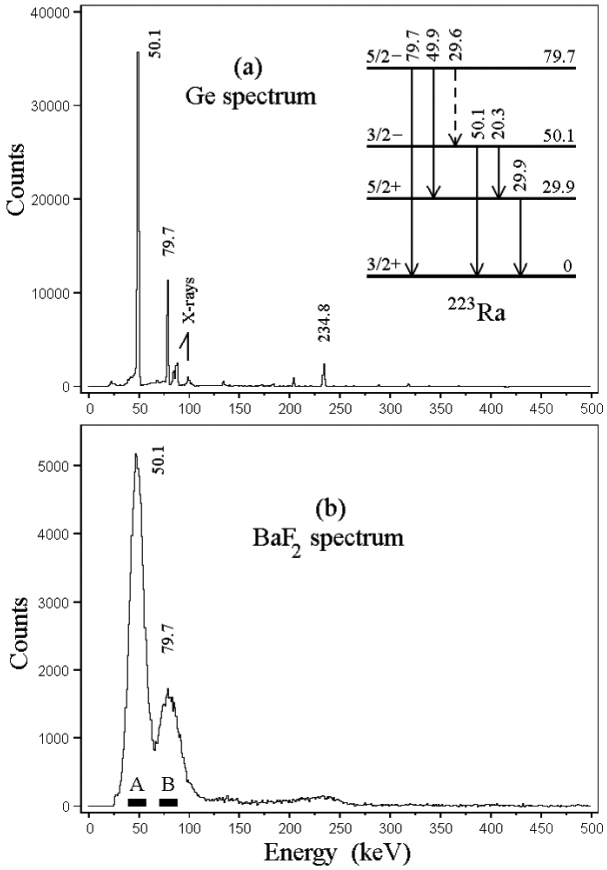

Fig. 1. β-gated γ-ray singles spectra recorded in the Ge and BaF_2 detectors (panels (a) and (b), respectively) following the β-decay of ^{223}Fr to ^{223}Ra. The impurity contribution from the β-decay of ^{223}Rn to ^{223}Fr has been subtracted the same way in both spectra. The inset to panel (a) shows a partial level scheme of ^{223}Ra, while, in panel (b), "A" and "B" label the gating regions selected for the 50.1 and 79.7 keV transitions. See text for further discussion.

of a very strong direct β feeding (70% and 15% [9]) to the 50.1 and 79.7 keV states in ^{223}Ra. The intensity of γ-rays from higher-lying states has been largely suppressed by β-gating, either due to absorption of low-energy β-rays in the material placed between the source and β detector, or were cut in the sorting procedure. The same purification procedure was applied for the β-BaF_2(t) coincidences. The β-gated ^{223}Ra γ-ray spectrum from the BaF_2 detector is shown in fig. 1(b). We used this spectrum to set a narrow gate on the 50.1 and 79.7 keV peaks (as shown in the figure by black rectangles "A" and "B"), in order to minimize the presence of other components (*e.g.* from a flat Compton background underneath the peaks).

The same purification procedure from the ^{223}Rn decay impurities has been applied in sorting the time-delayed spectra from the β-BaF_2(t) data. The time-delayed spectra for the 50.1 and 79.7 keV states in ^{223}Ra were sorted from the β-BaF_2(t) data (for batch-1 and batch-2) using one common gate on the β energy spectrum and gate "A" or "B" set on the BaF_2 energy spectrum. Then the proper fraction of the time-delayed spectra from batch-2 was subtracted from the spectra from batch-1 to remove impurities from the ^{223}Rn decay.

In the case of the time spectrum for the 50.1 keV level, the subtracted amount represented about 15% of the events. The process of subtraction affected predominantly the "prompt" part of the time-delayed spectrum, and thus it had small effect on its slope. Special care was taken to correctly assign the uncertainties to the content of each channel in the final time-delayed spectrum. The fitting was done to the whole time distribution and to the slope part alone, which was selected well outside the "prompt" region. Both fittings gave almost identical results, which indicates that the spectrum has predominantly one lifetime component. We note that relatively strong decay from the $5/2^-$ state at 79.7 keV feeds the $3/2^-$ state at 50.1 keV via a highly converted and fast intra-band $M1+E2$ transition of 29.6 keV [9], which brings a time-delayed component connected with the lifetime of the 79.7 keV level. However, this has a minor effect on the lifetime of the 3/2 state, since the ratio of the lifetimes is ~ 3, which is considered a "safe" ratio, see, *e.g.*, ref. [16]. Another difficulty is posed by the overlap of the γ-rays of energy 49.8 keV from the 79.7 keV state and 50.1 keV from the 50.1 keV level, see the insert to fig. 1(a). However, the 49.8 keV transition constitutes about 8.2% of the doublet [9]. Moreover, by fitting the time spectrum for the 50.1 keV level in the range from 0.8 ns to 8.0 ns, this impurity contribution is diminished to a marginal level of less than 0.5%. Nevertheless, a judicious allowance has been made for these factors by increasing the lifetime uncertainty of the $3/2^-$ state.

The analysis of the time-delayed spectrum for the 79.7 keV level has been done in a similar manner. Here the major impurity components are the X-rays mainly due to the strongly converted $M1$ transitions of energy 205.0 and 234.8 keV de-exciting the 234.9 keV state. However, our present data indicate that the lifetime of the 234.9 keV level is $T_{1/2} \leq 40$ ps, which is too short to cause interference in fitting the slope outside of the prompt region. Another, but very minor impurity, is a small overlap of the 50.1 and 79.7 keV peaks in the BaF_2 spectrum, see fig. 1(b), which means that there is a small presence of the time spectrum for the 50.1 keV level in the time distribution for the 79.7 keV level. Its presence is manifested at the level of ~ 10 counts in the 2 ns region of the spectrum. The final result quoted here for the 79.7 keV level is from fitting the spectrum over a region from 0.6 to 6.0 ns with two lifetime components, and with the second one fixed at $T_{1/2} = 587$ ps. (A free fit gives for the second component $T_{1/2} = 770(160)$ ps consistent with its origin as due to the 50.1 keV transition.)

Experimental time-delayed spectra for the 50.1 and 79.7 levels in ^{223}Ra shown in figs. 2 and 3 have slope on the delayed part, which appears for half-lives longer than ~ 40 ps. Figures also show the prompt Gaussian spectra and slope curves fitted in the de-convolution process. Time calibration was 13.07(4) ps/ch. The de-convolution of these two spectra gives $T_{1/2} = 587(12)$ ps and 210(13) ps for the $3/2^-$ and $5/2^-$ states at 50.1 and 79.7 keV, respectively. For these low energies the fitted prompt Gaussian

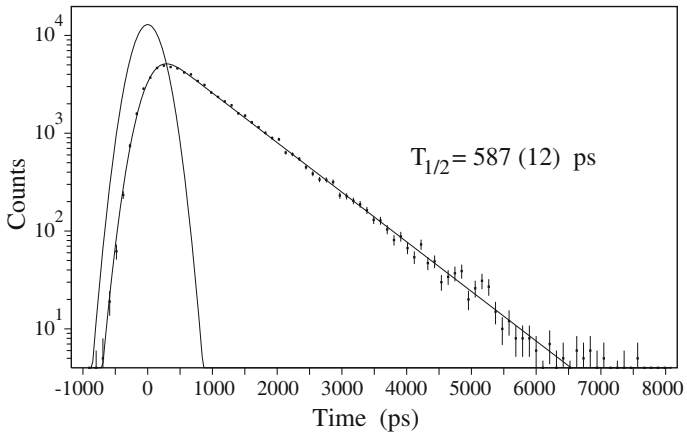

Fig. 2. Time-delayed $\beta\gamma$(t) spectrum gated by the 50.1 keV γ-ray (gate "A" in fig. 1(b)). The slope is due to the lifetime of the 50.1 keV level in ^{223}Ra.

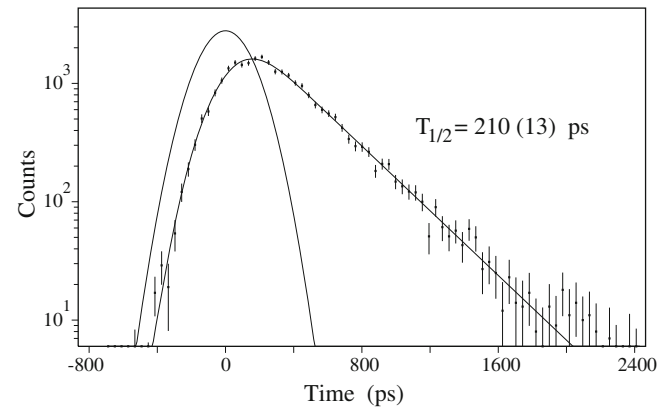

Fig. 3. Time-delayed $\beta\gamma$(t) spectrum gated by the 79.7 keV γ-ray (gate "B" in fig. 1(b)). The slope is due to lifetime of the 79.7 keV level in ^{223}Ra.

spectra have FWHM values of 500 ps and 350 ps, respectively and slopes of $T_{1/2} \sim 40$ ps. Obtained $T_{1/2}$ results are consistent with and more accurate than the previously measured values of 630(70) ps [3] and 166(55) ps ($\tau = 240(80)$ ps) [4], respectively. The new lifetime for the $3/2^-$ state at 50.1 keV, $T_{1/2} = 587(12)$ ps, which differs by almost 4 standard deviations from $T_{1/2} = 1070(130)$ ps, does not confirm this result listed in an internal report [14] and quoted in ref. [2].

Experimental reduced transition probabilities for γ-lines from the $K = 3/2$ doublet band in ^{223}Ra are given in table 1. For 50.1 and 79.7 keV levels they were calculated using half-lives measured in this work. For other levels half-lives from ref. [2] or calculated from the mean lifetimes τ of ref. [4] were used. Level energies, γ-ray energies, intensities and $\delta^2(E2/M1)$ mixing ratios used in table 1 are taken from ref. [9]. Total internal conversion coefficients $\alpha_{\rm TOT}$ are from ICC programme from the Radware Software Package (ref. [24]).

4 Discussion and conclusions

4.1 B(E1) rates

There are different approaches in describing octupole correlations in the nuclei from the $A \sim 225$ mass region [25]. When these correlations are very strong, a nucleus may possess stable octupole deformation and it can be described by including a nonzero octupole deformation parameter β_3 into the model calculations. In this case the strength of octupole interactions is described by the electric dipole moment $|D_0|$ (see sect. 4.2). When a nucleus has no stable octupole deformation, octupole correlations can be described in a dynamical way by octupole vibrations around the quadrupole deformed shape (see sect. 4.3). Moreover, one can describe them as the coherent quadrupole-octupole vibrations [13]. Octupole correlations can also be described by the cluster model in which the nucleus is treated as a composite system of spherical core plus light cluster [10–12].

Our calculations from sect. 4.3, in which the quasiparticle-phonon model was used, reproduce experimental reduced transition probabilities $B(E1)$ reasonably well (see table 1). The $B(E1)$ values in ^{223}Ra are also quite well reproduced by model of the coherent quadrupole and octupole motion [13] and by the cluster model [10].

4.2 Electric dipole moments D_0

We have used the experimental reduced transition probabilities $B(E1)$ given in table 1 to determine the electric dipole moments, D_0, evaluated using the standard rotational model formula:

$$B(E1; I_i \to I_f) = \frac{3}{4\pi} D_0^2 \, \langle I_i K_i 10 | I_f K_f \rangle^2 \, . \qquad (1)$$

Although this formula is not strictly applicable to the transitional nuclei (the energy ratio of the first excited 4^+ to the 2^+ states in ^{222}Ra is 2.71), it nevertheless provides consistent means for inter-comparison of the $B(E1)$ strength between even-even and odd-A nuclei as well as for the $E1$ transitions de-exciting various band members.

The D_0 values obtained from the experimental $B(E1)$ rates from table 1 are given in table 2. These values are much lower than expected for the center of octupole deformation region. The average D_0 value of 0.155(10) e·fm, deduced from our lifetime measurements for 50.1 and 79.7 keV levels, confirms the enhancement of octupole correlations for the $K = 3/2$ configuration compared to the lowest levels from the $K = 1/2$ and $K = 5/2$ configurations. However, the D_0 values for the higher spin states (7/2, 9/2, 11/2) of the $K = 3/2$ configuration are much lower than for the low spin members (see table 2).

We have calculated D_0 values corresponding to the theoretical $B(E1)$ rates obtained with the QPM model (table 1) and the quadrupole-octupole vibrational model of ref. [13]. These values together with the theoretical D_0 moments obtained with the shell-correction method based on the reflection-asymmetric Woods-Saxon model [1] are compared with the experimental D_0 values in fig. 4. The

Table 1. Level lifetimes and experimental and theoretical reduced transition probabilities for the $K = 3/2$ band in ^{223}Ra. Level energies, γ-ray energies and intensities and $\delta^2(E2/M1)$ mixing ratios (not mentioned) are taken from ref. [9].

Initial level [keV]	$I_i K_i^\pi$	$T_{1/2}$ [a] [ps]	E_γ [keV]	I_γ	$I_f K_f^\pi$	$X\lambda$	$\alpha_{\rm TOT}$	$B_{\rm exp}(X\lambda)$ [b]	$B_{\rm theor}(X\lambda)$ [b]
29.858	5/2 3/2$^+$	< 600	29.86(1)	100.0	3/2 3/2$^+$	$M1$	113.8	$> 3.7 \times 10^{-3}$	7.2×10^{-3}
						$E2$	3314	$> 9.9 \times 10^{3}$	8.1×10^{3}
50.128	3/2 3/2$^-$	587(12) [c]	20.25(5)	2.8(3)	5/2 3/2$^+$	$E1$	7.781	$1.28(14) \times 10^{-3}$	4.7×10^{-4}
			50.13(1)	100(5)	3/2 3/2$^+$	$E1$	0.707	$3.02(16) \times 10^{-3}$	1.21×10^{-3}
61.424	7/2 3/2$^+$	700(180)	31.58(1)	76(12)	5/2 3/2$^+$	$M1$	96.41	$4.1(15) \times 10^{-3}$	6.9×10^{-3}
						$E2$	2515	$4.6(17) \times 10^{3}$	4.6×10^{3}
			61.441(20)	100(12)	3/2 3/2$^+$	$E2$	98.39	$3.01(85) \times 10^{3}$	2.8×10^{3}
79.708	5/2 3/2$^-$	210(13) [c]	29.60(3)	0.3	3/2 3/2$^-$	$M1$	116.8	$1.12(7^{\rm (d)}) \times 10^{-2}$	1.32×10^{-2}
			49.82(5)	22(5)	5/2 3/2$^+$	$E1$	0.718	$1.91(45) \times 10^{-3}$	1.1×10^{-4}
			79.69(2)	100(4)	3/2 3/2$^+$	$E1$	0.205	$2.12(16) \times 10^{-3}$	2.0×10^{-4}
123.793	7/2 3/2$^-$	340(70)	44.22(12)	3.5(9)	5/2 3/2$^-$	$M1$	35.59	$5.9(20) \times 10^{-3}$	1.4×10^{-3}
						$E2$	481.9	$1.16(39) \times 10^{4}$	4.0×10^{3}
			62.45(5)	13.4(17) [e]	7/2 3/2$^+$	$E1$	0.393	$1.12(27) \times 10^{-4}$	3.9×10^{-5}
			73.63(5)	0.9(4)	3/2 3/2$^-$	$E2$	41.32	$1.10(54) \times 10^{3}$	2.7×10^{3}
			93.88(5)	100.0(22)	5/2 3/2$^+$	$E1$	0.132	$2.46(51) \times 10^{-4}$	7.2×10^{-4}
130.141	9/2 3/2$^+$	220(50)	6.5(3)	100(30)	7/2 3/2$^-$	$E1$	42.30	$1.11(42) \times 10^{-1}$	1.6×10^{-3}
			68.74(3)	64(12) [e]	7/2 3/2$^+$	$M1$	9.794	$4.5(13) \times 10^{-3}$	8.8×10^{-3}
						$E2$	57.40	$2.77(82) \times 10^{3}$	8.7×10^{3}
			100.27(3)	93(18)	5/2 3/2$^+$	$E2$	9.61	$3.6(11) \times 10^{3}$	4.2×10^{3}
174.569	9/2 3/2$^-$	120(30)	44.40(5)	0.7(8)	9/2 3/2$^+$	$E1$	0.978	$\sim 8.0 \times 10^{-5}$	2.4×10^{-6}
			50.85(5)	2.9(12)	7/2 3/2$^-$	$M1$	23.71	$1.71(93) \times 10^{-2}$	3.3×10^{-2}
						$E2$	245.5	$1.5(8) \times 10^{4}$	2.6×10^{3}
			94.97(5)	5(3) [e]	5/2 3/2$^-$	$E2$	12.39	$\sim 8.4 \times 10^{3}$	4.0×10^{3}
			113.11(5)	100	7/2 3/2$^+$	$E1$	0.363	$6.9(17^{\rm (d)}) \times 10^{-4}$	1.6×10^{-3}
174.58	11/2 3/2$^+$	140(42) [f]	44.40(5)	8(6)	9/2 3/2$^+$	$M1$	35.16	$\sim 2.7 \times 10^{-2}$	3.2×10^{-2}
			113.11(5)	100	7/2 3/2$^+$	$E2$	5.793	$2.25(68^{\rm (d)}) \times 10^{4}$	2.3×10^{3}
247.39	11/2 3/2$^-$	110	72.85(5)	12(10)	9/2 3/2$^-$	$M1$	8.264	$4.0(33^{\rm (d)}) \times 10^{-2}$	2.0×10^{-2}
			117.20(5)	100(8)	9/2 3/2$^+$	$E1$	0.332	$8.82(71^{\rm (d)}) \times 10^{-4}$	1.03×10^{-3}
			123.58(10)	7(3)	7/2 3/2$^-$	$E2$	3.968	$5.8(25^{\rm (d)}) \times 10^{3}$	4.7×10^{3}

[a] Half-lives are taken from ref. [2] except when noted otherwise.
[b] In units of e^2fm^2 for $E1$ transitions, e^2fm^4 for $E2$ transitions, μ_N^2 for $M1$ transitions and $\mu_N^2\,fm^2$ for $M2$ transitions.
[c] From this work.
[d] Only partial error, due to the lack of γ-ray intensity or $T_{1/2}$ errors.
[e] Undivided intensity of the double γ-line.
[f] Calculated from mean lifetime given in ref. [4].

D_0 moments from the QPM model which are derived from the intrinsic states of structure given in table 4 are quenched. They reproduce D_0 values only for states with $I = 11/2$ from the $K = 3/2$ configuration and with $I = 5/2$ from the $K = 5/2$ configuration. Octupole correlations for the $K = 3/2$ configuration are slightly enhanced compared to configurations with $K = 1/2$ and 5/2, however, the spin dependence of D_0 for the $K = 3/2$ configuration is not reproduced. The D_0 values from model of ref. [13] and from calculations of ref. [1] are also quenched however, neither configuration nor spin dependence of D_0 is properly reproduced.

Figure 5 shows systematics of experimental D_0 moments for radium isotopes. It is not as smooth as for the thorium nuclei (see fig. 10 in ref. [27]) but one can see that the D_0 moments in ^{223}Ra follow the general trend of D_0 values in radium isotopes. In contrast to thorium isotopes, fig. 5 shows a decrease of D_0 values for $222 \leq A \leq 225$. These isotopes lie in the center of octupole region in actinides where the strongest octupole correlations are expected. The D_0 values calculated from the theoretical $B(E1)$ rates from the QPM model and model of ref. [13] reproduce this quenching in ^{223}Ra. In the case of the reflection-asymmetric Woods-Saxon model

Table 2. Intrinsic dipole moments, $|D_0|$, for the $K = 3/2$ band, determined from the experimental $B(E1)$ rates in ^{223}Ra.

E_i [keV]	I_i^π K_i	E_γ [keV]	$I_f^\pi K_f$	$\|D_0\|$ [efm]
50.13	$3/2^-$ 3/2	20.25	$5/2^+$ 3/2	0.116(6)
		50.13	$3/2^+$ 3/2	0.145(4)
79.71	$5/2^-$ 3/2	49.82	$5/2^+$ 3/2	0.176(21)
		79.69	$3/2^+$ 3/2	0.182(7)
123.79	$7/2^-$ 3/2	93.88	$5/2^+$ 3/2	0.054(6)[(a)]
174.57	$9/2^-$ 3/2	44.40	$9/2^+$ 3/2	~ 0.061[(a)]
		113.11	$7/2^+$ 3/2	0.085(11[(b)])[(a)]
247.39	$11/2^-$ 3/2	117.20	$9/2^+$ 3/2	0.093(4[(b)])[(a)]

[(a)] Deduced using half-lives of ref. [2].
[(b)] Only partial error, due to the lack of γ-ray intensity or $T_{1/2}$ errors.

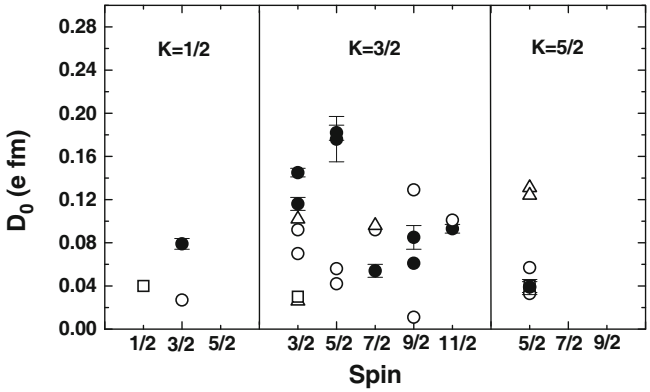

Fig. 4. Comparison of experimental (full circles) and theoretical (empty symbols) D_0 moments in ^{223}Ra. Experimental moments were deduced using level lifetimes measured in this work and in refs. [2,4]. Empty circles denote D_0 values calculated from the B(E1) rates obtained with the QPM model (see sect. 4.3) and empty triangles with the model of the coherent quadrupole-octupole vibrations [13]. Empty squares show values calculated in ref. [1] using reflection-asymmetric Woods-Saxon potential and shell-correction method.

this D_0 quenching is explained by the cancellation between the macroscopic and shell correction contributions to D_0 which have opposite signs [1]. In radium nuclei opposite signs of the $D_0^{\rm macr}$ and $D_0^{\rm shell}$ contributions are predicted for isotopes with $222 \leq A \leq 227$ [1]. In thorium nuclei small quenching is predicted only for isotopes $226 \leq A \leq 228$. Similar D_0 quenching is observed in ^{146}Ba [1] which lies in the center of the octupole region in lanthanides.

Recently, a novel method was applied at REX-ISOLDE in which Coulomb excitations with radioactive beams were used to study octupole correlations in ^{220}Rn and ^{224}Ra [26]. It allowed to determine electric dipole and octupole moments in studied nuclei. The latter moment seems to be important as it may help to distinguish if the octupole correlations in a nucleus are of vibrational nature or they arise from stable octupole deformation.

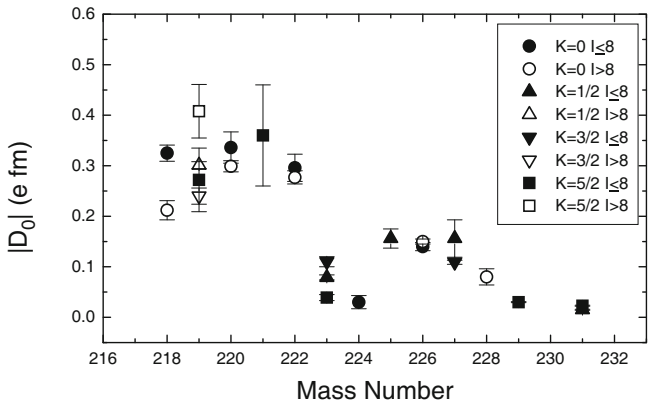

Fig. 5. Average electric dipole moments D_0 for radium isotopes. Full symbols denote average D_0 values for spins up to 8 and empty symbols for higher spins. The D_0 value for ^{221}Ra is taken from ref. [25] and for ^{223}Ra from this work. The D_0 moment for ^{224}Ra was calculated from experimental data given in ref. [26] and for other Ra isotopes from the data given in the NNDC data base [15].

4.3 Dynamical description of the octupole correlations

The low-lying states in nuclei from the region $Z \approx 87$–90 are known to be influenced by strong octupole correlations (see, *e.g.*, ref. [25]). In some particular nuclei from this region the octupole correlation can be sufficiently strong to create a stable octupole deformation of the nucleus mean field (with the nonzero electric dipole moment D_0 in the ground state —so-called strong octupole correlation limit). However more probably, the majority of nuclei from this region do not have a stable octupole deformation but the relatively strong octupole correlations lead only to high octupole vibration components in the low-lying states of these nuclei (dynamical description of the octupole correlations) (*e.g.*, refs. [18,19]). The best description of this dynamical octupole correlations is provided by the standard axially symmetric rotor model (RM) including Coriolis coupling, where the intrinsic degrees of freedom are described by the quasiparticle-phonon model, QPM, (see *e.g.*, refs. [18,19] and citations therein). This approach is discussed in details in ref. [18], therefore here only basic elements of it, needed for the understanding of further discussions, are given.

The RM approach starts with the nucleus Hamiltonian in the form

$$\hat{H} = \hat{H}_{\rm intr} + \hat{H}_{\rm rot}, \tag{2}$$

where $\hat{H}_{\rm rot}$ is given by

$$\hat{H}_{\rm rot} = \frac{\hbar^2}{2\mathcal{F}}\left[\hat{I}^2 + \hat{j}^2 - \hat{I}_3^2 - \hat{j}_3^2\right] - \frac{\hbar^2}{2\mathcal{F}}\left(\hat{I}_+\hat{j}_- + \hat{I}_-\hat{j}_+\right). \tag{3}$$

Here $\mathcal{F}$ is the moment of inertia with respect to the axis perpendicular to the symmetry axis; $\hat{I}_3$ and $\hat{j}_3$ are the projection operators of the total and intrinsic angular momenta $\hat{\boldsymbol{I}}$ and $\hat{\boldsymbol{j}}$ onto the symmetry axis, respectively; $\hat{I}_\pm = \hat{I}_1 \pm \hat{I}_2$ and $\hat{j}_\pm = \hat{j}_1 \pm \hat{j}_2$. The inclusion of the Coriolis coupling term (the last term in (3)) requires the matrix

of the total Hamiltonian (2) to be constructed and diagonalized within the space of symmetrized functions [28]

$$|IMK\rho\rangle = \sqrt{\frac{2I+1}{16\pi}}\left\{\mathcal{D}^I_{MK}|K\rho\rangle + (-1)^I\mathcal{D}^I_{MK}\hat{R}_1(\pi)\,|K\rho\rangle\right\}, \quad (4)$$

where $\mathcal{D}^I_{MK}$ are the Wigner functions of the Euler angles; $|K\rho\rangle$ is the eigenvector of the intrinsic Hamiltonian satisfying $\hat{H}_{\rm intr}|K\rho\rangle = E^{(\rm intr)}_\rho|K\rho\rangle$, and ρ are quantum numbers of the given intrinsic state with the projection K of the intrinsic angular momentum onto the symmetry axis. $\hat{R}_1(\pi)$ is a rotation by angle π around the first intrinsic axis. After the diagonalization of the total Hamiltonian matrix we obtain the energy levels $E_q(I)$ and the corresponding wave function

$$\hat{H}\,|IMq\rangle = E_q(I)\,|IMq\rangle,$$
$$|IMq\rangle = \sum_{K\rho} b^{Iq}_{K\rho}\,|IMK\rho\rangle, \quad (5)$$

where the index q characterizes given rotational band (intrinsic state above which given rotational band is built).

In our approach the intrinsic Hamiltonian is approximated by the QPM Hamiltonian [29]

$$\hat{H}_{\rm intr} \approx \hat{H}_{\rm QPM}, \qquad E^{(\rm intr)}_\rho \approx \eta_\rho, \qquad |K\rho\rangle \approx |\psi_K(\rho)\rangle, \quad (6)$$

where $|\psi_K(\rho)\rangle$ are the eigenvectors of the QPM Hamiltonian

$$\hat{H}_{\rm QPM}\,|\psi_K(\rho)\rangle = \eta_\rho\,|\psi_K(\rho)\rangle. \quad (7)$$

The QPM Hamiltonian involves the mean field $\hat{H}_{\rm sp}$ (Nilsson type, with only quadrupole deformation), the pairing residual interaction $\hat{H}_{\rm pair}$ (monopole type) and the long-range residual interaction $\hat{H}_{\rm res}$ in the quadrupole-quadrupole and octupole-octupole form [19,29]

$$\hat{H}_{\rm QPM} = \hat{H}_{\rm sp} + \hat{H}_{\rm pair} + \hat{H}_{\rm res}, \quad (8)$$

with

$$\hat{H}_{\rm res} = -\frac{1}{2}\sum_{\lambda=2,3}\sum_{\mu\geq 0}\kappa_{\lambda\mu}\,\hat{O}_{\lambda\mu}\hat{O}_{\lambda-\mu}, \quad (9)$$

where $\hat{O}_{\lambda\mu}$ are the isoscalar quadrupole ($\lambda = 2$) and octupole ($\lambda = 3$) single-particle operators. After the Bogoliubov transformation from single-particle operators to quasiparticle ones and using the RPA equations for one-phonon vibrational excitations of the even-even core, the intrinsic QPM Hamiltonian can be schematically rewritten in the form

$$\hat{H}_{\rm QPM} = \hat{H}_{\rm core} + \hat{H}_{\rm nQ}, \quad (10)$$

where $\hat{H}_{\rm core}$ generates phonon (vibrational) excitations of the double-even core, $\hat{H}_{\rm nQ}$ represents the coupling of odd-neutron (in the case of ^{223}Ra) with the vibrating double-even core. The explicit expressions for each of the terms involved in (10) are given, *e.g.*, in ref. [29], where one can find also their microscopic origin.

Table 3. Comparison of calculated and experimental quadrupole and octupole vibrational energies in ^{222,224}Ra (energies are given in keV).

^{224}Ra	$E_{\rm exp}(K^\pi = 0^+) = 916$	$E_{\rm QPM}(K^\pi = 0^+) = 992$
	$E_{\rm exp}(K^\pi = 2^+) = 965$	$E_{\rm QPM}(K^\pi = 2^+) = 984$
	$E_{\rm exp}(K^\pi = 0^-) = 216$	$E_{\rm QPM}(K^\pi = 0^-) = 292$
	$E_{\rm exp}(K^\pi = 1^-) = 1016$	$E_{\rm QPM}(K^\pi = 1^-) = 966$
^{222}Ra	$E_{\rm exp}(K^\pi = 0^+) = 914$	$E_{\rm QPM}(K^\pi = 0^+) = 880$
	$E_{\rm exp}(K^\pi = 2^+) = 1025$	$E_{\rm QPM}(K^\pi = 2^+) = 1106$
	$E_{\rm exp}(K^\pi = 0^-) = 242$	$E_{\rm QPM}(K^\pi = 0^-) = 325$

The search for the eigenvectors $|\psi_K(\rho)\rangle$ and eigenvalues η_ρ of the intrinsic QPM Hamiltonian (10) is usually performed in two steps. In the first step the RPA is used for the determination of the structure and energy of the quasiparticle phonon creation operators $Q^+_{\tilde{g}} = Q^+_{\lambda\mu i}$ ($\lambda = 2,3; \mu \geq 0; i$ enumerates individual RPA equation solutions). The strength constants $\kappa_{2\mu}$ and $\kappa_{3\mu}$ in (9) were determined from the systematic comparison of the lowest quadrupole (β- and γ- vibrations) and octupole vibration state energies in the double-even actinide nuclei (see ref. [29]). Primarily these constants were varied in order to obtain a good agreement of the calculated and experimental lowest quadrupole and octupole vibrational energies of the nearest double-even nuclei, that means vibrational states in ^{222}Ra and ^{224}Ra in our case. We have obtained a relatively good agreement with experiment, as shown in table 3 (experimental values were taken from ref. [15]).

In this comparison one should have in mind that optimal constants $\kappa_{\lambda\mu}$ cannot be far from systematic values for actinides given in ref. [29] and therefore, the agreement of experimental and calculated QPM cannot be more precise.

In the second step the interaction $\hat{H}_{nQ}$ between odd neutron and vibrating even-even core is taken into account in terms of the variational principle which determines the structure and energy of all eigenstates $|\psi_K(\rho)\rangle$ of the intrinsic QPM Hamiltonian $\hat{H}_{\rm QPM}$. The intrinsic wave function $|\psi_K(\rho)\rangle$ of odd-A nucleus has one-quasiparticle and one-quasiparticle-plus-phonon components given by [29]

$$|\psi_K(\rho)\rangle = \left[\sum_{\tilde{\nu}} C^{(\rho)}_\nu \alpha^+_{\tilde{\nu}} + \sum_{\tilde{\nu}\tilde{g}} D^{(\rho)}_{\tilde{\nu}\tilde{g}}\delta_{\tilde{\mu}+\tilde{K}_\nu,\tilde{K}_\rho}\alpha^+_{\tilde{\nu}}Q^+_{\tilde{g}}\right]|\rangle, \quad (11)$$

where $\alpha^+_{\tilde{\nu}} = \alpha^+_{\nu\sigma_\nu}$ represents the quasiparticle creation operator ($\sigma_\nu = \pm 1$ is the sign of the projection of the intrinsic angular momentum onto the symmetry axis). The first term in (11) is the sum over the one-quasiparticle components of valence quasiparticles which can be occupied by odd nucleon, $C^{(\rho)}_\nu$ is the amplitude of each

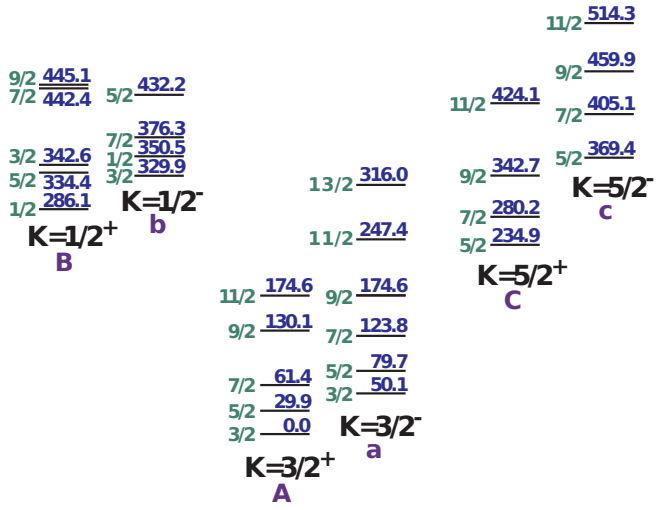

Fig. 6. Low-lying experimental spectrum of ^{223}Ra. Only experimentally recognized rotational bands are given (see ref. [15]). The bands are paired to the parity doublet bands A-a, B-b, C-c (see the text).

one-quasiparticle component. The second term in (11) involves the sum over all quasiparticle-plus-phonon components. $Q^+_{\tilde{g}} = Q^+_{\lambda\mu\sigma i}$ stands for the phonon creation operator of the vibrating nuclear core with the multipolarity λ and multipolarity projection $\tilde{\mu} = \mu\sigma$ ($\mu \geq 0$, $\sigma = \pm$). The index i enumerates the phonons with the same $\lambda\mu$. $D^{(\rho)}_{\nu\tilde{g}}$ represents the amplitude of the quasiparticle-plus-phonon component νg in the wave function (11). In each quasiparticle-plus-phonon component the angular momentum projection $\tilde{\mu}$ of the core phonon couples with the angular projection $\tilde{K}_\nu$ of the quasiparticle ν to the intrinsic angular momentum projection $\tilde{K}_\rho$ ($\tilde{K}_\rho = \tilde{\mu} + \tilde{K}_\nu$). The symbol $|\rangle$ stands for the product of the phonon vacuum and the vacuum for the valence quasiparticles which can be occupied by an odd nucleon (for further details of the QPM approach for odd-A nucleus see refs. [18,29]). Knowing the structure (11) of each intrinsic state and the amplitudes $b^{Iq}_{K\rho}$ in (5) the intraband and extraband reduced $E1$, $E2$, $M1$ transition probabilities can be calculated (see ref. [18] for details).

Calculated reduced probabilities of $E1$, $E2$ and $M1$ intraband and extraband transitions using the wave functions (5) are presented in the rightmost column of table 1. Detailed description of the calculation, including the discussion of the parameters of used RM+QPM Hamiltonian can be found in ref. [18]. The comparison of the calculated values of reduced probabilities from the last (10th) column with the corresponding experimental values given in the 9th column of table 1 shows the qualitatively good mutual agreement.

In the nucleus ^{223}Ra six rotational bands were interpreted in the experimental data (see ref. [15]). These bands can be divided into three parity doublet bands as is shown in fig. 6 ($K = 3/2\pm$ pair A-a, $K = 1/2\pm$ pair B-b, $K = 5/2\pm$ pair C-c).

Table 4. Structure of the low-lying intrinsic states in ^{223}Ra.

Band mark	Structure of the intrinsic state $\lvert\Psi_K(\rho)\rangle$	%	Bandhead energy (experimental) (keV)	Intrinsic energy (theoretical) $\eta - \eta_0$ (keV)
	$3/2[642]$	69.2		
	$3/2[631]$	0.8		
A	$3/2[761] + Q^+_{30}$	20.8		
	$3/2[512] + Q^+_{30}$	3.2		
	$3/2[751] + Q^+_{30}$	1.1	0.0	0.0
	$3/2[761]$	62.3		
	$3/2[642] + Q^+_{30}$	33.7		
a	$1/2[770] - Q^+_{22}$	1.5		
	$7/2[743] - Q^+_{22}$	0.5	50.1	290.2
	$5/2[633]$	67.1		
	$5/2[752] + Q^+_{30}$	25.1		
C	$1/2[631] + Q^+_{22}$	1.0		
	$11/2[725] - Q^+_{33}$	0.9		
	$9/2[734] - Q^+_{32}$	0.9	234.9	401.6
	$5/2[752]$	47.4		
	$5/2[503]$	2.5		
c	$5/2[633] + Q^+_{30}$	44.6		
	$1/2[770] + Q^+_{22}$	1.9		
	$3/2[642] + Q^+_{31}$	1.3	369.4	661.8
	$1/2[640]$	48.0		
	$1/2[651]$	33.9		
B	$1/2[770] + Q^+_{30}$	5.1		
	$1/2[510] + Q^+_{30}$	3.1		
	$1/2[750] + Q^+_{30}$	2.3		
	$1/2[521] + Q^+_{30}$	2.2	286.1	285.3
	$1/2[770]$	66.4		
	$1/2[501]$	6.3		
b	$1/2[640] + Q^+_{30}$	16.7		
	$3/2[761] - Q^+_{22}$	2.9		
	$1/2[651] + Q^+_{30}$	1.4		
	$5/2[752] - Q^+_{22}$	0.9	329.9	616.8
	$1/2[501]$	78.8		
	$1/2[770]$	5.1		
	$5/2[503] - Q^+_{22}$	4.4		
	$3/2[501] - Q^+_{22}$	3.7		
	$1/2[640] + Q^+_{30}$	2.7		
	$1/2[660] + Q^+_{30}$	1.0		~ 834
	$1/2[631]$	55.1		
	$1/2[651]$	7.9		
	$1/2[640]$	6.7		
	$1/2[501] + Q^+_{30}$	7.2		
	$1/2[761] + Q^+_{30}$	5.8		
	$1/2[770] + Q^+_{30}$	4.4		
	$5/2[633] - Q^+_{22}$	2.5		~ 930
	$5/2[503]$	87.2		
	$5/2[752]$	1.7		
	$1/2[501] + Q^+_{22}$	2.1		
	$5/2[632] + Q^+_{30}$	0.9		~ 960

If the nucleus has a stable octupole deformation, then the parity doublet bands are degenerate. As can be seen from fig. 6, both bands in each pair of parity doublet bands are relatively close to each other but not degenerate. That suggests that the nucleus ^{223}Ra does not have a stable octupole deformation in the lowest intrinsic states above which the rotational bands, shown in fig. 6, are built. Nevertheless, the analysis of the structure of intrinsic states corresponding to the given pair of doublet bands is indicative of the mutual octupole correlation between these intrinsic states. This can be seen from table 4 where for several lowest intrinsic states the composition of one-quasiparticle and quasiparticle-plus-phonon components (the second column) are presented with the square of the corresponding amplitudes ($|C_\nu^{(\rho)}|^2$ or $|D_{\tilde{\nu}\tilde{g}}^{(\rho)}|^2$) in the percentage with which the given component enters the normalization condition

$$\sum_{\tilde{\nu}} |C_\nu^{(\rho)}|^2 + \sum_{\tilde{\nu}\tilde{g}} |D_{\tilde{\nu}\tilde{g}}^{(\rho)}|^2 = 1 \qquad (12)$$

of each intrinsic state with the index ρ. The third column in table 4 contains the experimental bandhead energy of the corresponding rotational band built above the given intrinsic state (just for the identification of the given band in fig. 6). The 4th column shows the calculated differences between the intrinsic energy η_ρ of the given intrinsic state and the intrinsic energy η_{ρ_0} of the ground intrinsic state.

The identification of the parity doublets shown in fig. 6 is provided by the octupole correlations present in the intrinsic structure of the two partner bands in each parity doublet (see table 4) supported further by proximity in the level energies. More specifically, one observes a symmetry in the intrinsic structure of the partner bands: the dominant one-quasiparticle component of the first partner coupled to the octupole phonon of the core forms the largest collective component in the structure of the second partner, and vice versa. In such a way the QPM reflects the parity doublet structure which is characteristic feature of strong octupole coupling. Such an octupole coupling of two bands in parity doublet bands is characteristic in the lowest part of the spectrum also for other nuclei in the $Z \approx 87$–90 region (see, *e.g.*, refs. [18,19] and citations therein).

5 Summary

The electric dipole moments D_0 determined in this and earlier studies for ^{223}Ra are much lower than expected for the center of the octupole deformation region. The D_0 moments obtained from the half-lives measured in this work confirm much higher D_0 values for low spin states of the $K = 3/2$ configuration compared to the $K = 1/2$ and $5/2$ configurations, which implies strong configuration dependence of the $E1$ strength in the ^{223}Ra nucleus. These D_0 values are also much higher than those observed for higher-spin states from the $K = 3/2$ configuration. In our calculations using the quasiparticle-phonon model (QPM) the structure of the intrinsic states in ^{223}Ra was established. It allowed the observed rotational bands in this nucleus to divide into three parity doublet bands and to obtain reasonable values for the theoretical $B(E1)$ rates. The D_0 moments corresponding to these $B(E1)$ values are quenched and show enhancement of octupole correlations for the $K = 3/2$ configuration. However, they do not properly reproduce the spin dependence of experimental D_0 values for $K = 3/2$ configuration. Neither configuration nor spin dependence of D_0 is reproduced by other models.

This work was supported in part by the Swedish Natural Science Research Council, Norwegian Scientific Research Committee, the Nansen Foundation, the CICYT "Plan Nacional de Altas Energias" Spain (under contract AEN94-0833-C02-02), the U.K. Engineering and Physical Sciences Research Council, and the Polish Scientific Research Committee.

References

1. P.A. Butler, W. Nazarewicz, Nucl. Phys. A **533**, 249 (1991) and references therein.
2. Ch. Briancon, S. Ćwiok, S.A. Eid, V. Green, W.D. Hamilton, C.F. Liang, R.J. Walen, J. Phys. (London) G **16**, 1735 (1990).
3. H. Vartapetian, Compt. Rend. **246**, 1680 (1958).
4. C. Briancon, R. Walen, J. Phys. (Paris) **32**, 381 (1971).
5. S. Ćwiok, W. Nazarewicz, Nucl. Phys. A **529**, 95 (1991).
6. G.D. Jones, P.A. Butler, T.H. Hoare, P.M. Jones, Eur. Phys. J. A **2**, 129 (1998).
7. A. Abdul-Hadi, V. Barci, B. Weiss, H. Maria, G. Ardisson, Phys. Rev. C **47**, 94 (1993).
8. R.K. Sheline, Y. Chen, G.A. Leander, Nucl. Phys. A **486**, 306 (1988).
9. E. Browne, Nucl. Data Sheets **93**, 763 (2001).
10. B. Buck, A.C. Merchant, S.M. Perez, Nucl. Phys. A **634**, 15 (1998).
11. G.G. Adamian, N.V. Antonenko, R.V. Jolos, T.M. Shneidman, Phys. Rev. C **70**, 064318 (2004).
12. X.T. He, E.G. Zhao, W. Scheid, Int. J. Mod. Phys. E **15**, 1823 (2006).
13. N. Minkov, S. Drenska, K. Drumev, M. Strecker, H. Lenske, W. Scheid, Phys. Rev. C **88**, 064310 (2013).
14. J. Moraleès, C.F. Liang, Université de Zaragoza Report No. FAN/Z/2/74 (1974), unpublished.
15. National Nuclear Data Center, `www.nndc.bnl.gov/ENSDF/`.
16. H. Mach, R.L. Gill, M. Moszyński, Nucl. Instrum. Methods Phys. Res. A **280**, 49 (1989).
17. H. Mach, J. Billowes, M.J.G. Borge, D.G. Burke, P.A. Butler, J.F.C. Cocks, B. Fogelberg, S.J. Freeman, I.S. Grant, K. Gulda, G.D. Jones, E. Hagebø, P. Hoff, J. Hønsi, W. Kurcewicz, G. Løvhøiden, R.A. Naumann, K. Nybø,

G. Nyman, H. Ravn, B. Rubio, J. Simpson, A.G. Smith, J.F. Smith, K. Steffensen, J.L. Tain, O. Tengblad, T.F. Thorsteinsen, the ISOLDE Collaboration, in *Nuclear Shapes and Nuclear Structure at Low Excitation Energy*, edited by M. Vergnes, D. Goutte, P.H. Heenen, J. Sauvage (Editions Frontieres, Gif-sur-Yvette, 1994) p. 391, and the references therein.

18. A.J. Aas, H. Mach, M.J.G. Borge, B. Fogelberg, I.S. Grant, K. Gulda, E. Hagebø, W. Kurcewicz, J. Kvasil, A. Lindroth, T. Martínez, D. Nosek, B. Rubio, J.F. Smith, K. Steffensen, J.L. Taín, O. Tengblad, T.F. Thorsteinsen, Nucl. Phys. A **611**, 281 (1996).
19. A.J. Aas, H. Mach, J. Kvasil, M.J.G. Borge, B. Fogelberg, I.S. Grant, K Gulda, E. Hagebø, P. Hoff, W. Kurcewicz, A. Lindroth, G. Løvhøiden, A. Mackova, T. Martínez, B. Rubio, M. Sánchez-Vega, J.F. Smith, J.L. Taín, R.B.E. Taylor, O. Tengblad, T.F. Thorsteinsen, Nucl. Phys. A **654**, 499 (1999).
20. L.M. Fraile, A.J. Aas, M.J.G. Borge, B. Fogelberg, L.M. García-Raffi, I.S. Grant, K Gulda, E. Hagebø, W. Kurcewicz, J. Kvasil, G. Løvhøiden, H. Mach, A. Mackova, T. Martínez, B. Rubio, J.L. Taín, A.G. Teijeiro, O. Tengblad, T.F. Thorsteinsen, Nucl. Phys. A **657**, 355 (1999).
21. L.M. Fraile, M.J.G. Borge, H. Mach, R. Boutami, A.J. Aas, B. Fogelberg, L.M. García-Raffi, I.S. Grant, K Gulda, E. Hagebø, W. Kurcewicz, J. Kvasil, M.J. Lopez, G. Løvhøiden, T. Martínez, B. Rubio, J.L. Taín, O. Tengblad, Nucl. Phys. A **686**, 71 (2001).
22. E. Ruchowska, W.A. Płóciennik, J. Żylicz, H. Mach, J. Kvasil, A. Algora, N. Amzal, T. Bäck, M.J.G. Borge, R. Boutami, P.A. Butler, J. Cederkäll, B. Cederwall, B. Fogelberg, L.M. Fraile, H.O.U. Fynbo, E. Hagebø, P. Hoff, H. Gausemel, A. Jungclaus, R. Kaczarowski, A. Kerek, W. Kurcewicz, K. Lagergren, E. Nacher, B. Rubio, A. Syntfeld, O. Tengblad, A.A. Wasilewski, L. Weissman, Phys. Rev. C **73**, 044326 (2006).
23. W. Kurcewicz, I.S. Grant, K. Gulda, A.J. Aas, J. Billowes, M.J.G. Borge, D.G. Burke, P.A. Butler, J.F.C. Cocks, B. Fogelberg, S.J. Freeman, G.D. Jones, E. Hagebø, P. Hoff, J. Hønsi, A. Lindroth, G. Løvhøiden, H. Mach, T. Martínez, R.A. Naumann, K. Nybø, G. Nyman, H. Ravn, B. Rubio, J. Simpson, A.G. Smith, J.F. Smith, K. Steffensen, J.L. Taín, O. Tengblad, T.F. Thorsteinsen, Nucl. Phys. A **621**, 827 (1997).
24. D.C. Radford, Nucl. Instrum. Methods A **236**, 297 (1995).
25. P.A. Butler, W. Nazarewicz, Rev. Mod. Phys. **68**, 349 (1996) and references therein.
26. L.P. Gaffney, P.A. Butler, M. Scheck, A.B. Hayes, F. Wenander, W. Albers, B. Bastin, C. Bauer, A. Blazhev, S. Bönig, N. Bree, J. Cederkäll, T. Chupp, D. Cline, T.E. Cocolios, T. Davinson, H. De Witte, J. Diriken, T. Grahn, A. Herzan, M. Huyse, D.G. Jenkins, D.T. Joss, N. Kesteloot, J. Konki, M. Kowalczyk, Th. Kröll, E. Kwan, R. Lutter, K. Moschner, P. Napiórkowski, J. Pakarinen, M. Pfeiffer, D. Radeck, P. Reiter, K. Reynders, S.V. Rigby, L.M. Robledo, M. Rudigier, S. Sambi, M. Seidlitz, B. Siebeck, T. Stora, P. Thoele, P. Van Duppen, M.J. Vermeulen, M. von Schmid, D. Voulot, N. Warr, K. Wimmer, K. Wrzosek-Lipska, C.Y. Wu, M. Zielińska, Nature **497**, 199 (2013).
27. E. Ruchowska, W.A. Płóciennik, H. Mach, K. Gulda, B. Fogelberg, H. Gausemel, L.M. Fraile, W. Kurcewicz, K. Mezilev M. Sanchez-Vega, Eur. Phys. J. A **45**, 1 (2010).
28. A. Bohr, B.R. Mottelson, *Nuclear Structure*, Vol. **II** (Benjamin, N.Y., 1974).
29. V.G. Soloviev, *Theory of Complex Nuclei* (Pergamon, Oxford, 1976).